Journal of Fluids and Structures (2001) **15,** 941–954
doi:10.1006/jfls.2001.0390, available online at http://www.idealibrary.com on IDEAL®

COMPUTATION OF FORCE ON A CYLINDER IN A SHEAR FLOW

Y. Xu and C. Dalton*,†

Department of Mechanical Engineering, University of Houston Houston, TX 77204-4792, U.S.A.

(Received 15 January 2001, and in final form 14 February 2001)

This is a report of a numerical investigation of flow past a circular cylinder with the approach flow having a spanwise shear. A physical example of such a flow is a current with axial shear, flowing past a riser on an offshore platform. Computational results are reported for three Reynolds numbers (1 000, 10 000, and 20 000) with a shear parameter value of 0.0393. A 3-D spectral/finite-difference approximation was used, along with the Smagorinsky model in the large eddy simulation method, to solve the space-filtered version of the Navier–Stokes equations. Using the same numerical method, the shear-flow results are compared to the results for a uniform flow at the same Reynolds number. The effect of the shear is evident in the results, affecting both drag and lift coefficients. There is a slight axial dependence in the drag coefficients in the shear flow results, especially for increasing Reynolds numbers, at the different axial locations studied. The influence of shear on the lift coefficients at the same locations is not as strong. We attribute this to the secondary flow generated by the axial shear in the approach flow. Plots of axial and streamwise vorticity for both uniform and shear flows also demonstrate the differences in the two types of flow.

1. INTRODUCTION

Risers and tethers of offshore platforms are exposed to currents of varying magnitude and direction over their length. As such, the risers and tethers are subjected to vortex shedding which produces vortex-induced vibration (VIV). This vibration is difficult to predict even when the current is uniform and in only one direction. When the current varies along the axis of the cylinder and changes direction as well, the prediction of VIV is presently not feasible. Our purpose in this study is to present a method to compute the flow field for a cylinder in an axial shear flow. The capability of this prediction will eventually lead to the prediction of VIV for a cylinder in a shear flow.

There have been many studies that have examined the case of a uniform approach flow past a circular cylinder; one of the latest is by Williamson (1996). The uniform flow problem is fairly well understood from the flow physics point of view. Recent results by Lu *et al.* (1997) and Breuer (1999), using the large eddy simulation (LES) method, represent the present state of the art in doing 3-D high Reynolds number calculations for uniform approach flows past a cylinder. Lu *et al.* considered uniform approach flows to $\mathrm{Re} = 44\,200$ and obtained very good agreement with experimental data. For example, at $\mathrm{Re} = 44\,2000$, the calculated value of C_D was 1·2 and the r.m.s. value of C_L was 0·46 compared to experimental values of 1·2 and 0·48, respectively. Breuer presented results at $\mathrm{Re} = 140\,000$

* Now with Baker-Hughes, Houston, TX, U.S.A.
† dalton@uh.edu

0889–9746/01/070941 + 14 $35.00/0

and found reasonably good agreement with experimental results for C_D; however, results for C_L were not presented or discussed. Breuer did note one unusual behavior relating to convergence of the solution: decreasing the mesh size did not lead to improved accuracy in the results.

There have been several recent CFD studies which have used the solution of the 2-D Navier–Stokes equations to provide the input to ordinary differential equations to calculate the VIV oscillations of the cylinder. Meling (1998) used a 2-D finite-element procedure, with the one-equation turbulence model of Spalart and Allmans (1992) to calculate the uniform flow past a cylinder at $\mathrm{Re} = 21\,000$. In spite of using the 2-D description, Meling found excellent agreement between his calculated results and the experimental results of Moe *et al.* (1994) The instantaneous calculated results of Meling were used as the input to a pair of ordinary differential equations that described the response to vortex shedding. Schulz and Kallinderis (1998) also used a 2-D finite-element approach to describe the VIV behavior of a circular cylinder. Schulz and Kallinderis apparently did not use any turbulence modeling in their calculations; in spite of this, they presented results for Reynolds numbers as high as $4{\cdot}75 \times 10^5$, but apparently without experimental corroboration.

A problem even more challenging than the uniform approach flow problem is an approach flow with axial shear. When the current has a spanwise (axial) shear, the flow pattern around the cylinder could be influenced by the secondary flow generated by the leading-edge stagnation-pressure gradient. The secondary flow influences the vortex shedding over the cylinder length. To what extent vortex shedding is influenced is a function of the Reynolds number and the shear parameter $\beta = (D/U_o)(\partial u/\partial z)_{\max}$, where $(\partial u/\partial z)_{\max}$ is the maximum slope of the profile, D is the cylinder diameter, and U_o is the free-stream velocity determined by the average of the velocities over the cylinder span in question.

There have been several studies that examined the effect of shear in the approach flow on vortex shedding and the force that acts on a cylinder present in the flow. These studies have shown that a cellular shedding pattern has been observed along with a spanwise variation of the base pressure. Maull & Young (1973), in one of the earliest studies on the subject, noticed the spanwise variation of base pressure across the cellular wake structures in a linear shear flow past an airfoil-shaped body with a flat trailing edge. Mair and Stansby (1975) conducted essentially an extension of the Maull and Young study by performing similar experiments on relatively slender cylinders. Mair and Stansby found the base pressure to be a function of the mean Reynolds number and the shear parameter. Later experiments by Peltzer and Rooney (1981) with $0 < \beta < 0{\cdot}026$, and Peltzer (1982) reported a spanwise variation of base pressure, but seemingly without a relationship to a cellular pattern. Vandiver *et al.* (1996) studied the phenomenon of lock-in under highly sheared conditions. They found that, when the shear is high, lock-on was likely to occur because of the dominance of a single mode of vortex shedding over other modes. Mukhopadheyay *et al.* (1999) performed a direct numerical simulation of a linear shear flow past a circular cylinder at a mean Reynolds number of 131·5 and $\beta = 0{\cdot}2$. (At this value of Re, there is no turbulence present and the flow without shear is 2-D.) Their numerical results showed the same cellular shedding pattern as noted by previous investigations even at much higher values of Re, quite likely due to the relatively larger value of β.

2. MATHEMATICAL FORMULATION

For the present analysis, the fluid is considered to be viscous and incompressible. The Reynolds numbers for this effort are sufficiently large for the wake flow to be turbulent. Thus, the large eddy simulation (LES) method will be used to represent the fluid motion.

[See Lu *et al.* (1997) for details of LES applied to flow past a cylinder.] Since a spanwise shear flow produces a spanwise (z-direction) velocity component in the flow field near the cylinder, the basic flow field is 3-D and not just due to the turbulence present.

The governing equations for this effort are the continuity equation and the Navier–Stokes equation in general coordinates. The physical space is (x_1, x_2, x_3) and the computational space is (ξ_1, ξ_2, ξ_3). In general coordinates, the continuity equation is

$$\frac{\partial \bar{U}_m}{\partial \xi_m} = 0. \tag{1}$$

Also, in general coordinates, the Navier–Stokes equation in LES form is

$$\frac{\partial (J^{-1}\bar{u}_i)}{\partial t} + \frac{\partial}{\partial \xi_m}(\bar{U}_m \bar{u}_i) = -\frac{\partial}{\partial \xi_m}\left(J^{-1}\frac{\partial \xi_m}{\partial x_i}\bar{P}\right) + \frac{\partial \sigma_i^m}{\partial \xi_m} + \frac{2}{\mathrm{Re}}\frac{\partial}{\partial \xi_m}\left(G^{mn}\frac{\partial \bar{u}_i}{\partial \xi_n}\right), \tag{2}$$

where $\mathrm{Re} = U_o D/v$ and J^{-1} is the inverse of the Jacobian which is

$$J^{-1} = \det(\partial x/\partial \xi_m), \quad i = 1, 2, 3, \; m = 1, 2, 3. \tag{3}$$

Also, in equation (2), we have the following definitions:

$$\bar{U}_m = J^{-1}\frac{\partial \xi_m}{\partial x_i}\bar{u}_i, \; G^{mn} = J^{-1}\frac{\partial \xi_m}{\partial x_j}\frac{\partial \xi_n}{\partial x_j}, \tag{4a, b}$$

$$\sigma_i^m = v_T G^{mn}\frac{\partial \bar{u}_i}{\partial \xi_n}. \tag{4c}$$

In equations (1) and (2), the velocity u_i is called the resolved velocity field with the subgrid scale effects to be modeled, in this case, by the Smagorinsky (1963) method. For the simulations here, the physical space is represented by $(x_1, x_2, x_3) = (x, y, z)$ and the computational space by $(\xi_1, \xi_2, \xi_3) = (\xi, \eta, z)$, where ξ, η and z correspond to the general radial, circumferential and spanwise directions, respectively. Thus, we have

$$J^{-1} = x_\xi y_\eta - x_\eta y_\xi. \tag{5}$$

In equation (4c), the eddy viscosity term, v_T, is represented by the Smagorinsky (1963) model for the subgrid scale stresses,

$$v_T = 2C_s^2 \Delta^2 (2\bar{S}_{ij}\bar{S}_{ij})^{1/2}, \tag{6}$$

where

$$\bar{S}_{ij} = \frac{1}{2}\left(\frac{\partial \xi_m}{\partial x_j}\frac{\partial \bar{u}_i}{\partial \xi_m} + \frac{\partial \xi_m}{\partial x_i}\frac{\partial \bar{u}_j}{\partial \xi_m}\right),$$

C_s is a constant, specified *a priori*, and Δ is the cube root of the product of the three mesh spacings. A value of C_s equal to 0.1 was used for these calculations.

3. BOUNDARY AND INITIAL CONDITIONS

The approach flow to the cylinder is described as a sinusoidal flow over the computational length of the cylinder. This approach flow is shown in Figure 1 where the approach velocity is given by

$$U(z) = U_o - U_p \sin(2\pi z/L), \tag{7}$$

where U_o is the mean velocity, U_p is the maximum velocity in the sinusoidal wave, and L is the wavelength of the approach flow. The approach velocity is chosen to have a sinusoidal

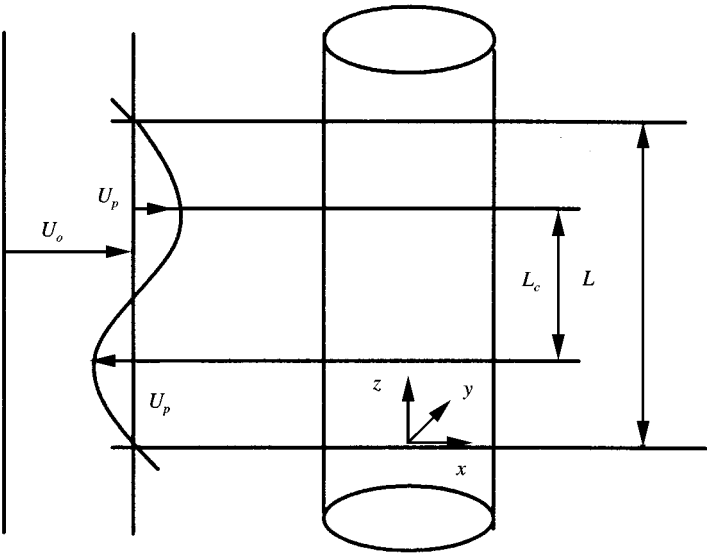

Figure 1. Flow configuration and coordinate system.

variation because of the periodic boundary conditions that are available at $z = 0, L$. If a linear shear flow were chosen to represent the approach flow, it would not be possible to prescribe boundary conditions at $z = 0, L$ with an open axial boundary at each location. The presence of a stagnation pressure gradient along the leading edge of the cylinder due to the change in approach velocity in a linear shear flow means that the flow at any given value of axial coordinate is an unknown, 3-D flow because of the secondary flow generated. Therefore, z-direction boundary conditions at $z = 0, L$ cannot be specified for a linear shear flow with open boundaries at these two locations. In contrast, specifying the approach flow as sinusoidal, as in Figure 1, means that the boundary conditions at $z = 0, L$ can be specified. Whatever the flow is at $z = 0, L$, it is the same. Thus, periodic boundary conditions can be prescribed at these two locations. Thus, the z-direction boundary conditions at $z = 0, L$ are

$$\bar{u}_i(\xi, \eta, 0) = \bar{u}_i(\xi, \eta, L), \qquad i = 1, 2, 3,$$

$$\bar{P}(\xi, \eta, 0) = \bar{P}(\xi, \eta, L). \tag{8}$$

Mukhopadhyay *et al.* (1999) used a linear shear flow in their calculations. However, a different type of boundary condition was used at $z = 0, L$. They used end plates in their model so that no flow (i.e., secondary flow) crossed the computational boundaries in the z-direction. We considered this approach, but decided to leave the axial boundaries open; hence, we used the sinusoidal approach velocity.

The boundary conditions on the surface of the cylinder are

$$\bar{u}_i(1, \eta, z) = 0, \qquad i = 1, 2, 3. \tag{9}$$

The boundary conditions in the circumferential direction are periodic,

$$\bar{u}_i(\xi, \eta, z) = \bar{u}_i(\xi, \eta + 2\pi, z), \qquad i = 1, 2, 3,$$

$$\bar{P}(\xi, \eta, z) = \bar{P}(\xi, \eta + 2\pi, z). \tag{10}$$

Outflow boundary conditions must be specified so that vortices can pass the outflow boundary unhindered by the presence of the boundary. These boundary conditions are not a trivial issue since they can influence the inner flow by the incompressible nature of the fluid. Many researchers, such as Gresho & Sani (1987) and Mittal & Balachandar (1994) have discussed these outflow boundary conditions. However, there is not yet a firm agreement about what these outflow boundary conditions should be to provide an accurate solution. Our position on the outflow boundary conditions is the following:

$$\frac{\partial^2 \bar{u}_i}{\partial \xi^2} = \frac{\partial \bar{u}_i}{\partial \xi} = 0, \qquad i = 1, 2, 3. \tag{11}$$

These outflow boundary conditions are applied to that part of the boundary at or near where vortices cross the boundary which is determined from preliminary calculations and depends on the Reynolds number. The remaining part of the far-field boundary is considered to have undisturbed flow crossing it. These outflow boundary conditions allow the vortices to cross the outflow boundary undisturbed as will be seen in the results to be presented.

The computational length of the approach flow is in the region indicated by L in Figure 1. However, the region over which we will examine results is specified by the length L_c ($= L/2$). It is within this region that the approach vorticity for the flow described in equation (7) is of constant sign. This is what is needed for the secondary flow generated by the leading-edge stagnation-pressure gradient to be in the negative z-direction.

4. FORCE DESCRIPTION

Determination of the velocity field allows the instantaneous force to be calculated from an integration of the circumferential pressure and vorticity distributions on the cylinder surface. Nondimensionalizing the drag and lift forces by $\frac{1}{2}\rho U_o^2 D$ to obtain the drag and lift coefficients, we get

$$\bar{C}_D = \int_0^{2\pi} y_\eta \bar{P} \mathrm{d}\eta - \frac{2}{\mathrm{Re}} \int_0^{2\pi} x_\eta \omega_z \mathrm{d}\eta \tag{12}$$

and

$$\bar{C}_L = -\int_0^{2\pi} x_\eta \bar{P} \mathrm{d}\eta + \frac{2}{\mathrm{Re}} \int_0^{2\pi} y_\eta \omega_z \mathrm{d}\eta. \tag{13}$$

In equations (12) and (13), the first integral is the force contribution due to the pressure distribution and the second integral is the force due to the shear stress. The average over the length L_c ($L/4 \le z \le 3L/4$) is a straightforward computation; the averages are

$$\bar{C}_D = \frac{1}{(L/2)} \int_{L/4}^{3L/4} \int_{\eta_{\min}}^{\eta^{\max}} y_\eta \bar{P} \mathrm{d}\eta \, \mathrm{d}z - \frac{2}{(L/2)\mathrm{Re}} \int_{L/4}^{3L/4} \int_{\eta_{\min}}^{\eta^{\max}} x_\eta \omega_z \mathrm{d}\eta \mathrm{d}z \tag{14}$$

and

$$\bar{C}_L = -\frac{1}{(L/2)} \int_{L/4}^{3L/4} \int_{\eta_{\min}}^{\eta^{\max}} x_\eta \bar{P} \mathrm{d}\eta \, \mathrm{d}z + \frac{2}{(L/2)\mathrm{Re}} \int_{L/4}^{3L/4} \int_{\eta_{\min}}^{\eta^{\max}} y_\eta \omega_z \mathrm{d}\eta \mathrm{d}z, \tag{15}$$

where the term ω_z, the spanwise vorticity, is based on the resolved velocities.

5. NUMERICAL SOLUTION

To discretize the governing equations, we use a combined spectral/finite-difference approximation. A Fourier spectral description is used in the axial direction and a finite-difference approximation is used in the plane parallel to the direction of the approach flow. The convective terms are represented by a third-order upwinding scheme. A multigrid method was used to solve the finite-difference form of the equations.

We use a second-order fractional step method (FSM) to advance the governing equations in time. In this approach, we first find an intermediate velocity by omitting pressure and using the second-order Adams–Bashforth scheme on the convective terms and the Crank–Nicolson scheme on the viscous terms. This intermediate velocity is corrected by pressure, which is obtained through a Poisson equation, to satisfy the continuity equation. Finally, the boundary conditions on velocity are applied to obtain the velocity at the next time step. [See Lu *et al.* (1997) for the details of the FSM used herein.]

6. RESULTS

The method described in the previous sections has been applied to the problem of a flow with a spanwise shear past a fixed circular cylinder. The approach flow has been described with a sinusoidal component imposed on a current with a fixed mean value. As stated earlier, the approach flow is sinusoidal because of the convenience of the boundary conditions at $z = 0, L$. However, because of the desire to examine the flow only in regions of shear of like sign, we will present results in the range of z given by $L/4 \leq z \leq 3L/4$. We will compare calculations of drag and lift results for both uniform flow and a sinusoidal shear flow. These comparisons are done for Re $= 1\,000$, $10\,000$, and $20\,000$ with the shear flow parameter, $\beta = (D/U_o)(\partial u/\partial z)_{\max}$, equal to 0.0393. This value of shear parameter corresponds to $U_p/U_o = 0{\cdot}025$ and the velocity varies from $0{\cdot}975U_o$ to $1{\cdot}025U_o$ over the length L_C.

The mesh for Re $= 1000$ is $129 \times 129 \times 16$ (ξ, η, z) and the time step is $\Delta t = 0{\cdot}005$. For Re $= 10\,000$ and $20\,000$, the mesh is $129 \times 193 \times 16$ (ξ, η, z) and $\Delta t = 0{\cdot}0025$. The length of the cylinder shown in all the vorticity plots is the length L_c which, in these calculations, was $2D$. The total computational length was $4D$. A convergence test was done at Re $= 20\,000$ and the results of that test will be presented in that section.

6.1. Results For Re $= 1000$, $\beta = 0.0393$

Figures 2 and 3 show vorticity patterns for this case for both the streamwise and axial vorticity distributions. Figure 2 shows a comparison of the streamwise vorticity, ω_r, for a uniform approach flow and a shear flow. The effect of the shear is clearly evident on the fore part of the cylinder with three cells plainly visible. The uniform flow result, in contrast, has no structure on the fore part of the cylinder. The near wake of the shear flow calculation has features that are distinct from the uniform flow calculation. The far wake is less distinct between the two situations, but there is still a difference in the axial structure of the streamwise far wake vortical structures. Figure 3 shows the axial vorticity, ωz, which indicates far less difference between the two different approach flows.

Figure 4 shows the drag and lift coefficients, averaged over the length L_c ($L/4 \leq z \leq 3L/4$ in Figure 1), for both uniform and shear flow cases. Once the flow has become established at a dimensionless time of about 60, the drag and lift coefficients develop a fairly regular pattern for both cases. The calculated mean value of the drag coefficient at Re $= 1000$ is about 1.07, while the experimental value at this Reynolds number is 1.05. Comparing these values is not a true test of convergence; but, for an unsteady flow, it is an adequate test and

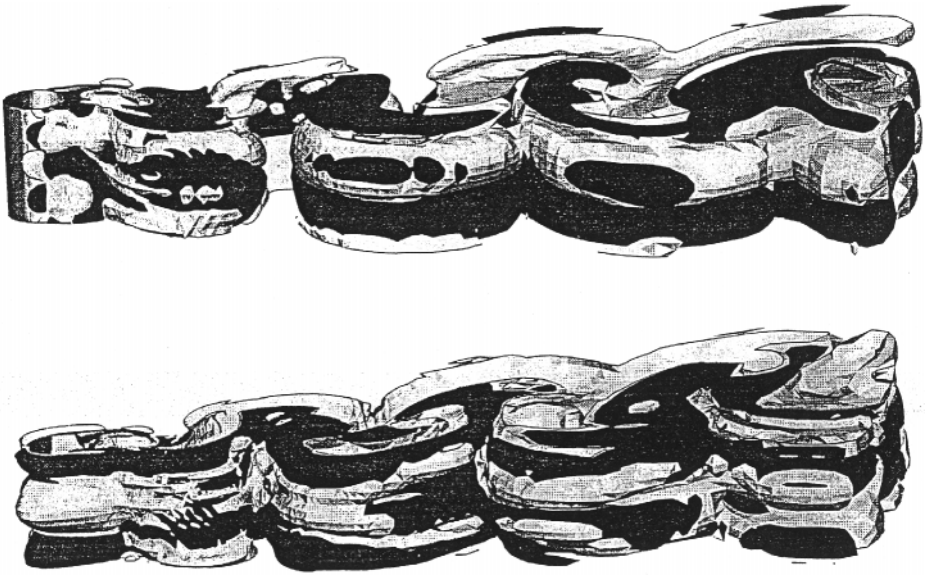

Figure 2. Streamwise vorticity distribution at Re = 1 000. Top: uniform flow; bottom: shearflow.

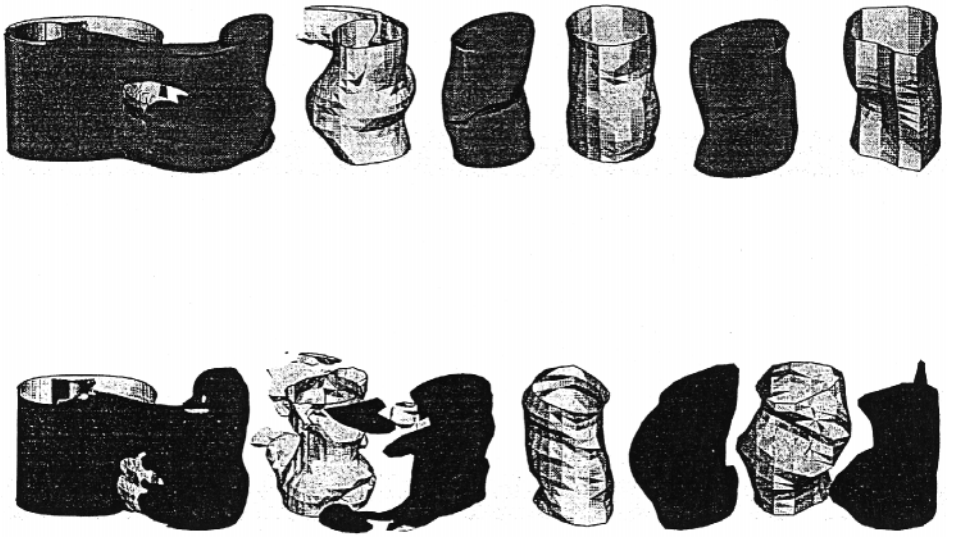

Figure 3. Axial vorticity distribution at Re = 1 000. Top: uniform flow; bottom: shear flow.

perhaps the only test available, in the absence of extensive statistical data in the wake which is not available for such flows. The onset of vortex shedding is triggered numerically and the onset is dependent on mesh size. Therefore, a comparison of results at different mesh sizes at the same computational time will more than likely have a phase difference even though the same mean drag is produced. With such a phase difference, it is not possible to make any comparisons at the same computational time. This issue has been discussed by Lu *et al.* (1997). However, even at the same mesh size, there is a phase difference between the uniform

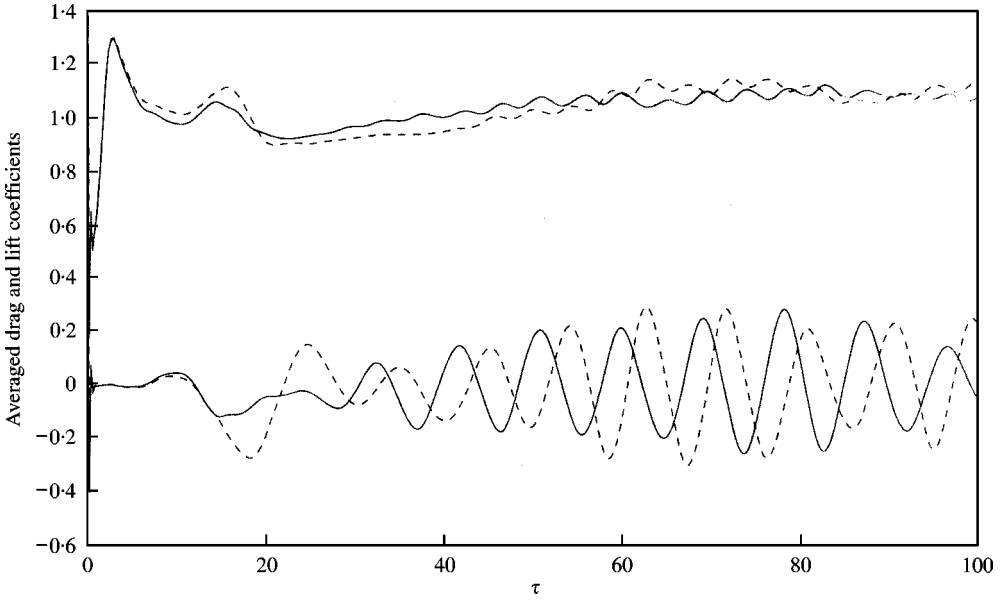

Figure 4. Length-averaged C_D and C_L versus time at Re = 1 000: ———, uniform flow; – – – – –, shear flow.

and shear flow plots in both the drag and lift signals. There is also evidence of a higher harmonic in the shear flow case. Figure 5 shows a plot of the drag and lift coefficients at three different locations along the length of the cylinder for the shear flow case. The drag plot shows more of an effect of location than the lift plot. According to equation (7), the dimensionless velocity at $z = 3L/8$ is 0·965; at $z = L/2$, it is 1·0; and at $z = 5L/8$, it is 1·035. These velocities produce such slight variation in the value of Re that essentially no change in C_D should be expected in the 2-D sense. However, Figure 5 shows a decrease in the value of C_D with increasing velocity, but with virtually no phase difference in the calculated results. The value of C_D at the highest point is 1·05, 1.1 at the midpoint, and 1.15 at the lowest point. There is a slight phase shift present in the drag plot as well as a magnitude difference at the extremes of the region being compared. The lift plot shows a very slight magnitude difference, also with no phase difference at the three locations. This result also indicates that the vortex shedding at the three different z locations is in phase. We suggest that this in-phase behavior of C_D and C_L at the three different axial positions is due to the secondary flow (the z-direction velocity) which is the result of the shear flow. This secondary velocity, which is in the negative z-direction, seems to be sufficient to cause axially correlated vortex shedding over the computational region at this value of the shear parameter.

6.2. Results For Re = 10 000, $\beta = 0{\cdot}0393$

The vorticity patterns for this case are compared in Figures 6 and 7. Figure 6 shows the streamwise vortical structure for both types of flows. The uniform approach flow, having no upstream vorticity, has no streamwise vortical structure until the formation of the separated shear layer leading to the shedding of the wake vortices. The vortical structure in the shear flow is quite evident on the front part of the cylinder due to the vorticity present in the approaching flow. The wakes of the two flows are quite similar, however, with little distinct

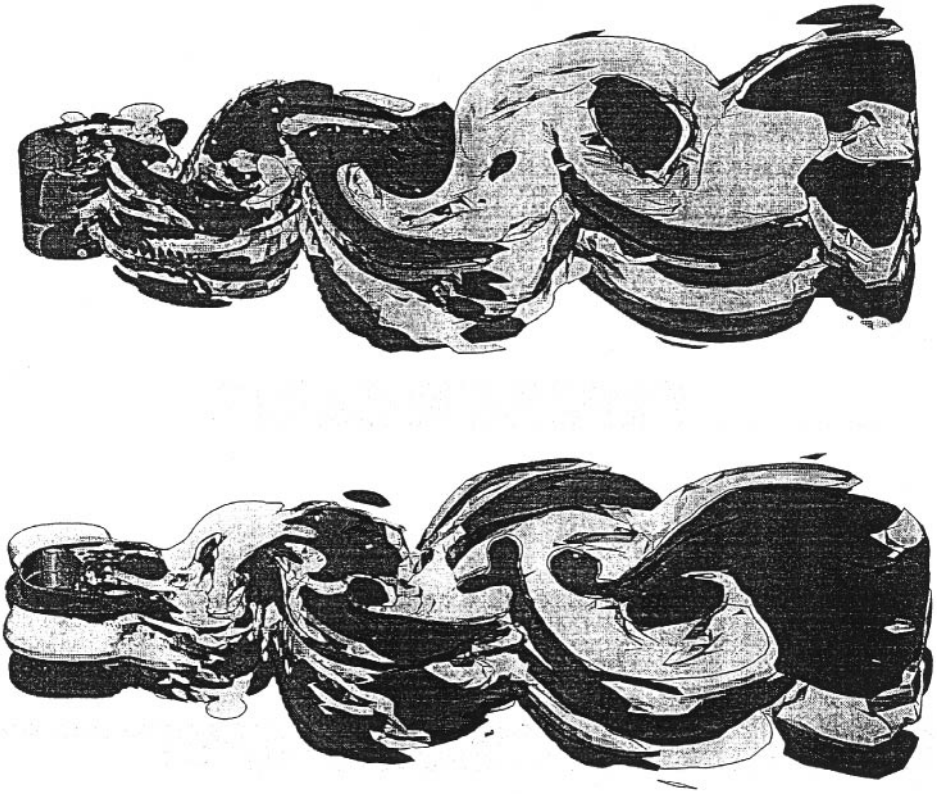

Figure 6. Streamwise vorticity distribution at Re = 10 000. Top: uniform flow; bottom: shear flow.

Figure 7. Axial vorticity distribution at Re = 10 000. Top: uniform flow; bottom: shear flow.

doi:10.1006/jfls.2001.0390

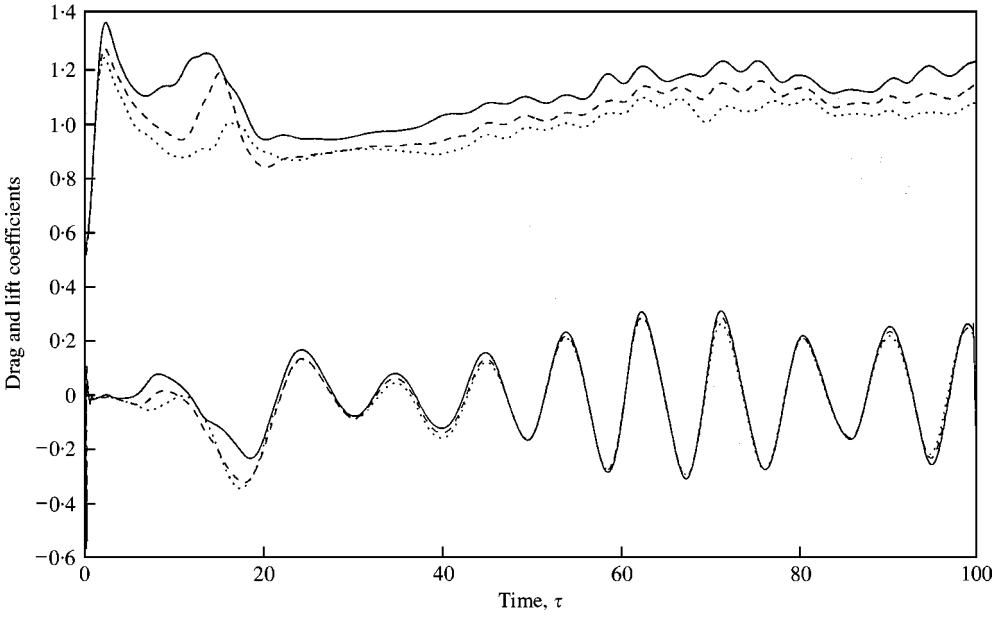

Figure 5. C_D and C_L versus time at three different axial positions at Re = 1 000: ———, $z = 3L/8$; – – – – –, $z = L/2$; ……, $z = 5L/8$.

difference between them. The axial vorticity is shown in Figure 7 for both uniform and shear flows. There is a cellular pattern present in the uniform flow result which is expected due to the axial variation of vortex shedding even in a uniform flow. The cellular pattern is even more noticeable in the shear flow plot, especially in the far wake where some of the fine vortical structure has been damped through the effects of viscosity.

Figure 8 shows the drag and lift coefficients, averaged over the length L_c. The uniform-flow drag coefficient is about 1·25 which agrees with the experimental value of 1·2. The length-averaged shear-flow drag coefficient, at this Reynolds number, does not have as consistent a behavior as the length-averaged uniform-flow drag coefficient. We surmise that the secondary flow generated by the leading-edge stagnation pressure gradient is affecting the base pressure. This behavior has a smoothing effect on the length-averaged drag coefficient. This is also evident in the length-averaged lift coefficient where a "phase difference" has developed in the uniform-flow and shear-flow results. This is not really a phase difference since these two flows are not the same; instead, the difference in the plot indicates a slightly larger value of the Strouhal number for the spatially averaged shear flow result.

Figure 9 shows the drag and lift coefficients for the shear flow at three different axial positions. The drag coefficient plots are essentially in phase from about $t = 30$. The lowest point again produces the highest value, $C_D = 1{\cdot}3$, while the two higher locations yielded $C_D = 1{\cdot}25$. The drag calculations are in phase, as was the case for Re = 10 000. The lift coefficients are also in phase and vary slightly in peak value. The in-phase behavior again suggests a correlated vortex-shedding pattern over the computational length of $4D$ taken for this analysis.

6.3. Results For Re = 20 000, $\beta = 0{\cdot}0393$

Figures 10 and 11 show the streamwise and axial vorticity distributions for this last case. The plot of the streamwise vorticity distributions in Figure 10 shows the effects on

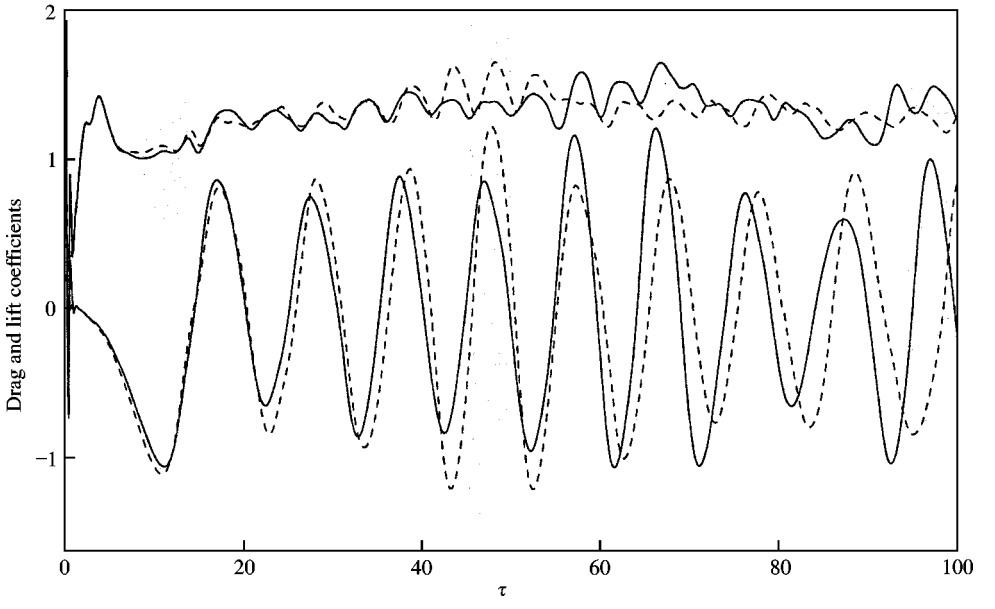

Figure 8. Length-averaged C_D and C_L versus time at Re = 10 000: ———, uniform flow; – – – – –, shear flow.

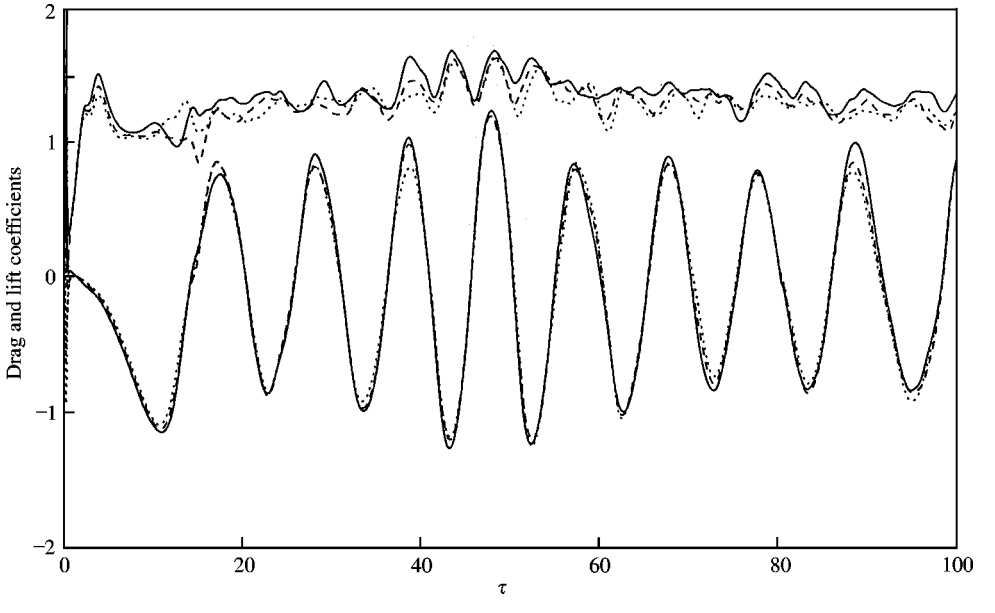

Figure 9. C_D and C_L versus time at three different axial positions at Re = 10 000: ———, $z = 3L/8$; – – – – –, $z = L/2$; . . . . ., $z = 5L/8$.

the fore part of the cylinder of the vorticity in the approach flow. The mixing in the wake for the shear-flow case is more prominent than in the uniform-flow case. Figure 11 shows how the uniform-flow and shear-flow axial vorticity patterns compare. The vortical structure in the separated shear layer for the approaching flow with shear is

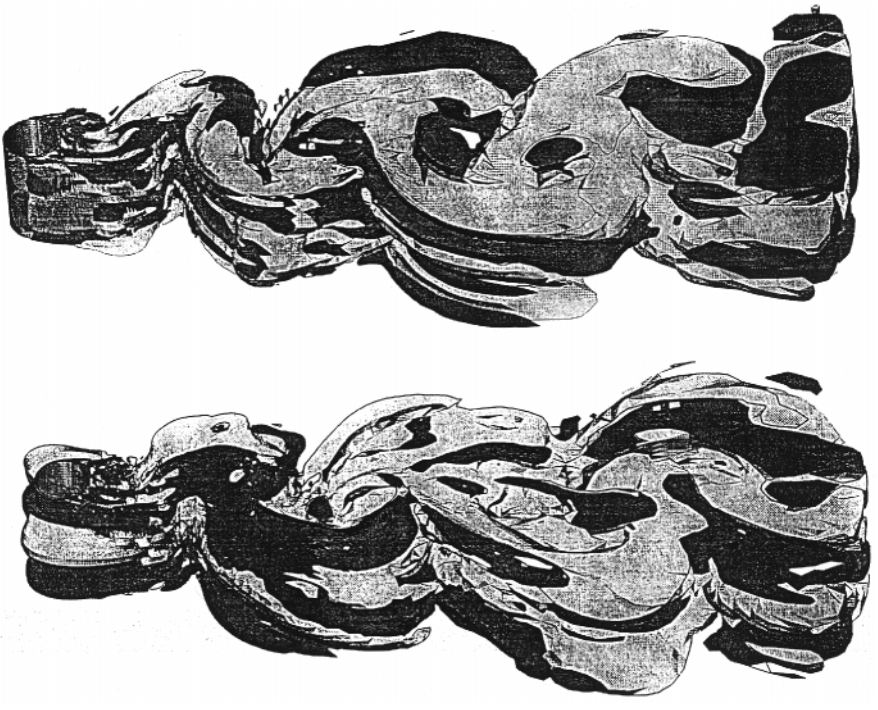

Figure 10. Streamwise vorticity distribution at Re = 20 000. Top: uniform flow; bottom: shear flow.

Figure 11. Axial vorticity distribution at Re = 20 000. Top: uniform flow; bottom: shear flow.

doi:10.1006/jfls.2001.0390

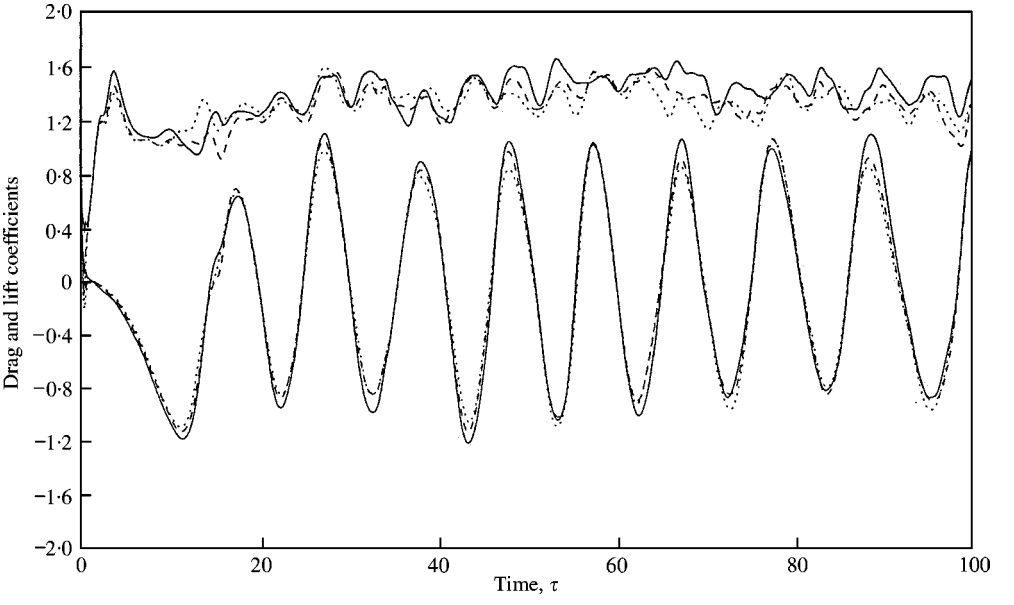

Figure 12. C_D and C_L versus time at three different axial positions at Re = 20 000: ———, $z = 3L/8$; – – – – –, $z = L/2$; ....., $z = 5L/8$.

irregular, while the same separated shear layer in the uniform flow case is relatively smooth. After the vortical structures have been shed, the flow patterns in both the near and far wakes are quite distinct. However, the far wake is much less distinct between the two cases which is an indication of the turbulent mixing present and the decay of the secondary flow generated by the stagnation pressure gradient on the fore part of the cylinder.

Figure 12 shows the drag and lift coefficients at three different locations in the range ($L/4 \leq z \leq 3L/4$). As for the two lower Reynolds numbers, the lift coefficient results are essentially in phase, but again with a very slight magnitude difference. However, at this highest Reynolds number, the drag coefficient plot shows the same trends as at Re = 10 000. The highest value ($C_D = 1{\cdot}3$) is again at the lowest position while the two higher locations yielded $C_D = 1{\cdot}25$. These C_D plots are again essentially in phase from about $t = 30$. As before, C_L is in phase for each of these locations with only a slight variation in peak values.

The absence of any phase difference in the lift coefficients at various positions along the cylinder length could be a numerical artifact due to the computational length being too short. So, we have investigated the computational length effect on the lift coefficients by doubling the length L_c on which the comparisons are made. Figure 13 shows the lift coefficient at the center section of the cylinder for two cases, $L_c = 2D$ and $4D$. There is only a slight effect present due to the increased computational length. Thus, we feel that our previously stated comment about the secondary flow having a strong influence on the phase behavior is valid and the longitudinal correlation of vortex shedding is enhanced, at least for the set of parameter values in this study.

Figure 14 shows the results of a convergence test performed at Re = 20 000. We have compared the drag and lift coefficients at two different mesh sizes, $129 \times 193 \times 16$ and $193 \times 225 \times 16$ (ξ, η, z). The results are virtually the same once a steady flow pattern is achieved, with a slight phase difference in the lift coefficient due to a slight mesh-size effect on wake instability at the onset of vortex shedding. Even though this is a global comparison

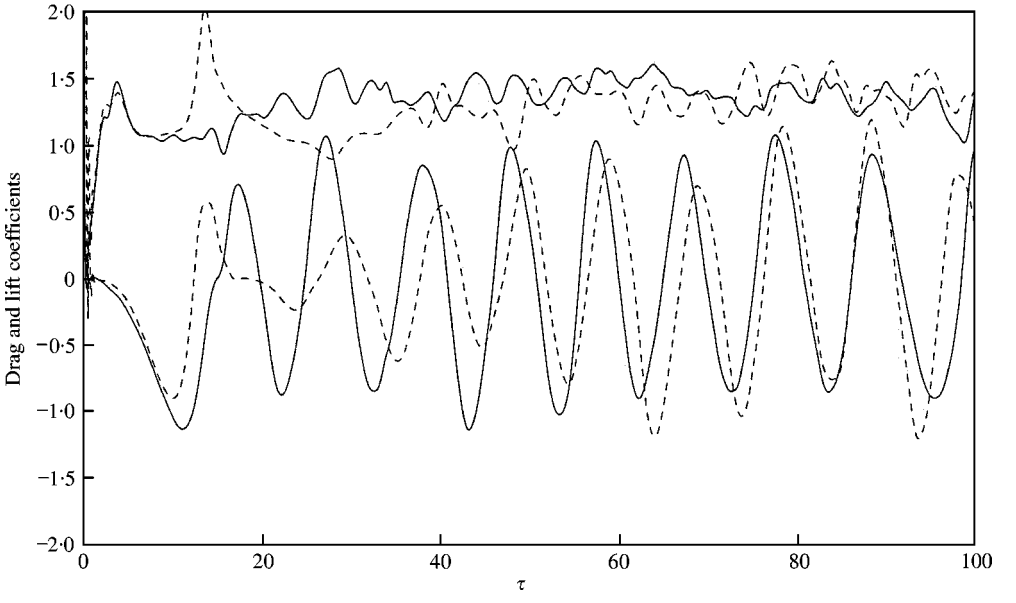

Figure 13. Sectional drag and lift coefficients of the shear flow at $z = L/2$ for $\mathrm{Re} = 20\,000$ with two different lengths of cylinder: ———, $L_C = 2D$; – – – – –, $L_C = 4D$.

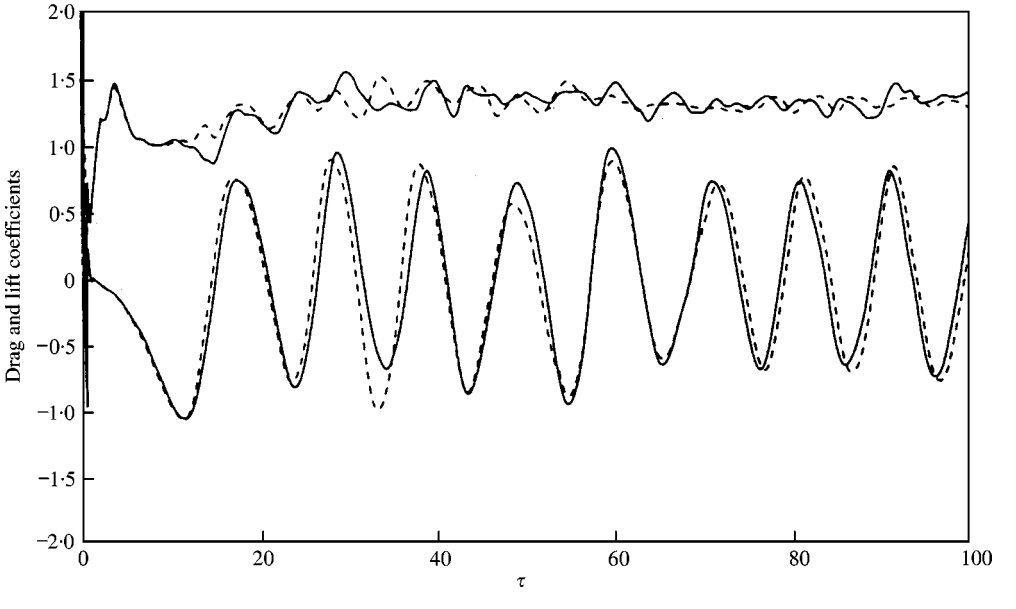

Figure 14. Convergence test for uniform flow at $\mathrm{Re} = 20\,000$: ———, $129 \times 193 \times 16$; – – – – –, $129 \times 225 \times 16$.

as opposed to a comparison of the actual numerical solutions, it must suffice because it is not meaningful to compare the numerical solutions in a highly time-dependent problem such as this.

7. CONCLUSIONS

This numerical investigation has shown a difference in the vorticity patterns and the drag and lift coefficients between approach flows with axial shear and no axial shear. Our code has been validated for the uniform flow case at each of the three Reynolds numbers studied. The vortical patterns shown in the figures are distinct and show a clear difference between the two approach flows and between the shear flow results as the Reynolds number increases. The drag coefficient in the shear flow results has a slight axial dependence. The length-averaged drag coefficients for the shear-flow cases has smoothed the axial effects and is somewhat different in character from the drag coefficients at each of the axial locations represented. The only noticeable difference in the length-averaged lift coefficients is a phase difference between the uniform-flow and shear-flow results at the two higher Reynolds numbers. We suggest that the in-phase behavior of the lift coefficients is due to the secondary flow generated on the fore part of the cylinder, at least for the parameters involved in this numerical study.

Since this problem has obvious interest to the offshore industry, additional calculations and experiments are needed over several values of the shear parameter and for several other Reynolds numbers to gain a better understanding of the effect of shear on drag, lift, and vortex shedding.

ACKNOWLEDGEMENTS

Support for this work was provided by the State of Texas Advanced Technology Program through Grant No. 003652-019. Supercomputer time was provided by the University of Houston on the NEC SX3 machine. Dexter Hill of NEC provided some time on the NEC SX4 machine in The Woodlands, TX. We are grateful to both organizations for the computer time.

REFERENCES

BREUER, M. 1999 A challenging test case for large eddy simulation high Reynolds number circular cylinder flow. *Proceedings*, *Turbulence and Shear Flow Phenomena*, Santa Barbara, CA.

GRESHO, P. M. & SANI, R. L. 1987 On pressure boundary conditions for the incompressible Navier–Stokes equations. *International Journal for Numerical Methods in Fluids* **7,** 1111–1145.

LU, X., DALTON, C. & ZHANG, J. 1997 Application of large eddy simulation to flow past a circular cylinder. *ASME Journal of Offshore Mechanics and Arctic Engineering* **119,** 219–225.

MAIR, W. A. & STANSBY, P. K. 1975 Vortex shedding from bluff cylinders in shear flow. *SlAM Journal of Applied Mathematics* **28,** 519–540.

MAULL, D. J. & YOUNG, R. A. 1973 Vortex shedding from bluff bodies in a shear flow. *Journal of Fluid Mechanics* **60,** 401–409.

MELING, T. S. 1998 Numerical prediction of the response of a vortex-excited cylinder at high Reynolds numbers. *Proceedings*, 17*th ASME Conference on Offshore Mechanics and Arctic Engineering*, Lisbon, OMAE paper no. 98–0315.

MITTAL, R. & BALACHANDAR, S. 1994 Study of flow over an elliptic cylinder using a direct numerical simulation. In *ASME Turbulence in Complex Flows*, FED-Vol. 203, pp. 11–19.

MOE, G., HOLDEN, K. & YTTERVOLI, P. O. 1994 Motion of spring-supported cylinders in subcritical and critical water flows. *Proceedings*, *Fourth International Offshore and Polar Engineering Conference*, pp. 468–475.

MUKHOPADHYAY, A., VENUGOPAL, P. & VANKA, S. P. 1999 Numerical study of vortex shedding from a circular cylinder in linear shear flow. *ASME Journal of Fluids Engineering* **121,** 460–468.

PELTZER, R. D. & ROONEY, D. M. 1981 Wake characteristics of high aspect ratio cylinders in subcritical spanwise sheared flow. ASME Paper no. 81-WA/FE-10.

PELTZER, R. D. 1982 Vortex shedding from a vibrating cable with attached spherical bodies in a linear shear flow. Naval Research Lab Memorandum Report 4940, Bethesda, MD, U.S.A.

SANI, R. L. & GRESHO, P. M. 1994 Resume and remarks on the open boundary condition mini-symposium. *International Journal for Numerical Methods in Fluids* **18,** 983–1008.

SCHULTZ, K. & KALLINDERIS, Y. 1998 Numerical prediction of vortex-induced vibrations. *Proceedings*, 17*th ASME Conference on Offshore Mechanics and Arctic Engineering*, *Lisbon*, OMAE paper no.98–0362.

SMAGORINSKY, J. 1963 General circulation experiments with the primitive equations; I. Basic experiments. *Monthly Weather Review* **91,** 99–164.

SPALART, P. R. & ALLMANS, S. R. 1992 A one-equation turbulence model for aerodynamic flow. AIAA paper no.92–0439.

VANDIVER, J. K., ALLEN, D. & LI, L. 1996 The occurrence of lock-on under highly sheared conditions. *Journal of Fluids and Structures* **10,** 555–56.

WILLIAMSON, C. H. K. 1996 Vortex dynamics in a cylinder wake. *Annual Review of Fluid Mechanics* **28,** 477–539.